Proposed Image-Processing Workflow for Wall-Corner Alignment Assessment under QLASSIC

Mohd Fadli Abdul Aziz [1], Muhammad Herman Jamaluddin[2*] and Ahmad Zaki Shukor[2]

[1]Sony EMCS Sdn. Bhd., Lot 5, Jalan Kemajuan, Bangi Industrial Estate, Bandar Baru Bangi, Selangor, Malaysia

[2]Faculty of Electrical Technology and Engineering, Universiti Teknikal Malaysia Melaka, Durian Tunggal, Melaka, Malaysia

***Corresponding Author**

DOI: https://doi.org/10.47772/IJRISS.2026.101000296

Received: 14 October 2026; Accepted: 19 October 2026; Published: 02 November 2026

ABSTRACT

This study examines the overall process of inspecting the internal wall finishes of a structure, focusing primarily on the evaluation of wall corner alignment. The present QLASSIC procedure was reviewed with attention to potential operator-dependent variation in the single-point manual assessment of internal wall-corner alignment. The review considers whether image-based measurement could complement the L-shaped ruler and steel-wedge procedure while retaining the existing acceptance criterion. A 4 mm error tolerance was deemed acceptable for assessing the alignment of wall corners. Thus, this review examines image-processing options for a future wall-corner alignment assessment method. A literature-informed conceptual workflow is proposed for subsequent implementation and controlled validation. The workflow was synthesized from the reviewed image-processing literature and is not presented as a validated replacement for the manual procedure. As wall corners are typically formed at the intersection of two walls, these will produce a straight line, which is vital information when capturing the image of a wall corner for analysis. Within the conceptual workflow, the Canny edge operator is identified as a candidate for preserving line information during edge extraction. The Hough line transform is likewise considered as a candidate method for extracting line orientation from the detected edges; its measurement performance remains to be established experimentally.

Keywords: Canny Edge Operator, Hough Line Transform, QLASSIC, Building Assessment, Wall Corner

INTRODUCTION

Quality assurance plays a significant role in building construction since user satisfaction and safety would be assured through proper quality inspection systems and procedures while reducing defects and maintenance costs (Olanrewaju et al., 2021). The standard technique and guideline adopted for quality assessment in Malaysia is the quality assessment system in construction (QLASSIC) (Yap et al., 2020). For evaluating wall alignment, the standard measurement tools are (200 mm x 300 mm) L-square frame and (0 mm - 6mm) steel wedge (CIDB, 2021). The evaluation for inspecting walls that meet at the right angle measures the gap between the L-square and the wall corner. However, the present method tends to be inconvenient and inaccurate, as measurement error may be introduced while maintaining the L-square frame horizontally and tightly to the wall (Yan et al., 2019).

One way to automatically inspect wall alignment while also meeting the criteria set by CIDB was to use a machine vision system, and there has been extensive research regarding the inspection system by using a visual sensor (Spencer et al., 2019; Tan et al., 2021; Tan et al., 2022). For example, previous works showed that wall detection could be determined by applying edge segmentation techniques to wall images and interpreting the wall edge line using Hough Transform (Arnaud et al., 2018; Song et al., 2017). However, most previous studies focused on detecting wall surface conditions, the wall localization process, or wall recognition without serious consideration for improving the current method of accessing wall alignment.

The traditional method of assessing wall alignment for construction buildings is less accurate and contains some errors. These errors may come from mishandling assessment tools, such as placing the L-square shape with slight skewness and improper gap measurements. Besides, the manual procedure is a labor-intensive and time-consuming process. The recent technology trends also contribute to further studies of the modern approach to building assessment methodology. Most of the previous studies included vision or laser sensors combined with a computational algorithm for quality evaluation of building construction.

Automated construction-quality inspection has already been demonstrated using mobile robots, cameras, depth sensors, laser scanners, point clouds, unmanned aerial vehicles, and building information modelling. However, the reviewed literature provides limited direct validation of a calibrated laser-line image workflow against the specific CIS 7 internal wall-corner criterion of a maximum 4 mm gap over a 300 mm L-square baseline. The resulting gap is therefore narrowly defined: evidence is still required to connect image formation, calibration, laser-line extraction, angular resolution, uncertainty, and a traceable physical reference to this QLASSIC acceptance rule.

A new approach for wall alignment inspection was proposed in this study, with the assessment including the evaluation of the angle between two walls at a corner. The foundation idea for the new assessment methodology was to use a vision system to capture images of the wall corners and image processing techniques were used. Necessary image operations, such as Canny edge detection with Standard and Probabilistic Hough Transform, were considered for line feature extraction.

Computer vision and image processing techniques have become increasingly valuable in the industrial sector, especially in manufacturing. The evolving technology has already taken place in many applications such as inspection, monitoring, measurement, and verification. The construction industry could also benefit from the integration of technology (Cheah et al., 2021). For example, a visual sensor with image processing proves to be more efficient and accurate than manual inspection.

An efficient autonomous system must accurately identify the parameters for the assessment. Therefore, an experimental setup for obtaining the data for analysis must be developed. In the proposed future implementation, the input data would be an image of a laser line projected onto the wall corner. The experimental design and selection of hardware are therefore identified as requirements for future implementation and validation. The present paper focuses on the literature-derived image-processing and feature-extraction workflow and does not report hardware implementation or measurement accuracy. Therefore, all the information for designing this project was elaborated further in this paper.

REVIEW SCOPE AND EVIDENCE BASE

This paper presents a focused narrative review and conceptual synthesis. It is not reported as a systematic review or meta-analysis. The evidence base combines the original image-processing literature retained in Appendices A–D with recent journal studies, principally from 2022–2025, on robotic inspection, depth sensing, laser scanning, point-cloud measurement, camera-pose control, UAV–BIM integration, and construction quality control. Sources were selected for their relevance to geometric inspection, traceable measurement, and the proposed QLASSIC use case.

The review asks three bounded questions: (1) which sensing and automation approaches have recently been used for construction quality inspection; (2) which geometric, calibration, and uncertainty requirements must be satisfied before image-derived line orientations can represent a physical wall-corner angle; and (3) what experimental evidence would be needed to evaluate a laser-line Canny–Hough workflow against the CIS 7 criterion. The synthesis supports design choices for future development and does not constitute experimental validation.

QUALITY ASSESSMENT SYSTEM IN CONSTRUCTION (QLASSIC)

The term QLASSIC is also known as Construction Industry Standard (CIS 7), originally introduced back in 2006. It is a standard system for assessing and evaluating construction projects based mostly on work quality

that falls under CIDB regulations in Malaysia. There are several criteria on which the building assessment processes focus: architectural works, material and functional tests, basic mechanical and electrical (M&E) fittings, and external works. Several aspects comprise the internal finishes evaluation, including the assessment of the internal wall, floor, door, ceiling, window, and internal fixtures. Again, the internal wall finishes will be evaluated based on a variety of criteria, including finishing, alignment and evenness, cracks and damage, hollowness, and jointing. The QLASSIC assessment tool list is included in Table 1 below, with its utilization.

For assessing the wall alignment, the method implemented by QLASSIC was to make sure the internal wall meets at a right angle using the L-square and steel wedge within a tolerance of 4 mm over 300 mm, as shown in Figure 1 below. In other words, the gap between the wall and the 300 mm side of the L-shaped ruler must be within 4 mm of the maximum allowable tolerance.
To better understand the process, Figure 2 shows a top view of the assessment process to measure alignment. The L-Square has two sides, one 300 mm and the other 200 mm. Using a steel wedge, they have a tolerance of 4 mm for the L-square side of 300 mm. Hence, converting to angle accuracy, the calculation for angle tolerance can be described as:

$$\tan^{-1}\left(\frac{4\text{ mm}}{300\text{ mm}}\right) = 0.7639° \quad (1)$$

Table 1. QLASSIC Assessment Tools.

No	Tools	Usage
1	Tapping Rod	To determine the hollowness of the wall when swiped on the surface
2	Stainless Steel L-Square	To measure the alignment of the wall, the door, and frame corners maintained at a right angle, and also for measuring tile lippage.
3	Steel Wedge	To measure the alignment of the wall, the door, and frame corners maintained at a right angle. Also, for measuring the tile lippage and wall verticality. Mainly for measuring gaps and evenness.
4	Steel Rule/Gauge	For gap measurement
5	Angle Mirror	For assessment of paintworks
6	Spirit Level	For measuring alignment and evenness
7	Measuring Tape	Mainly for measuring gaps and joints.

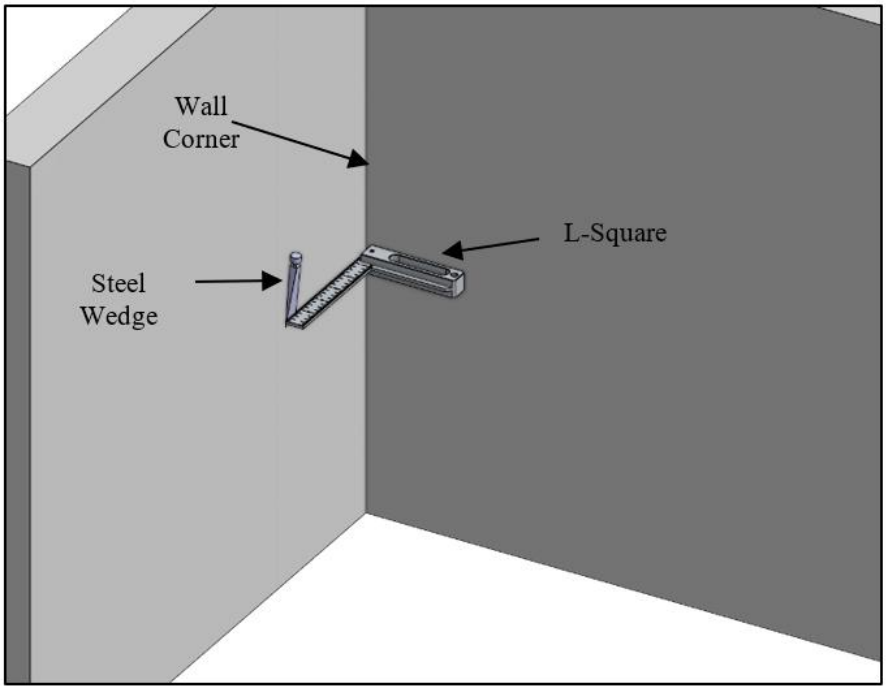

Figure 1. QLASSIC Internal Wall Alignment Assessment Method.

ISSN No. 2454-6186 | DOI: 10.47772/IJRISS | Volume X Issue X October 2026

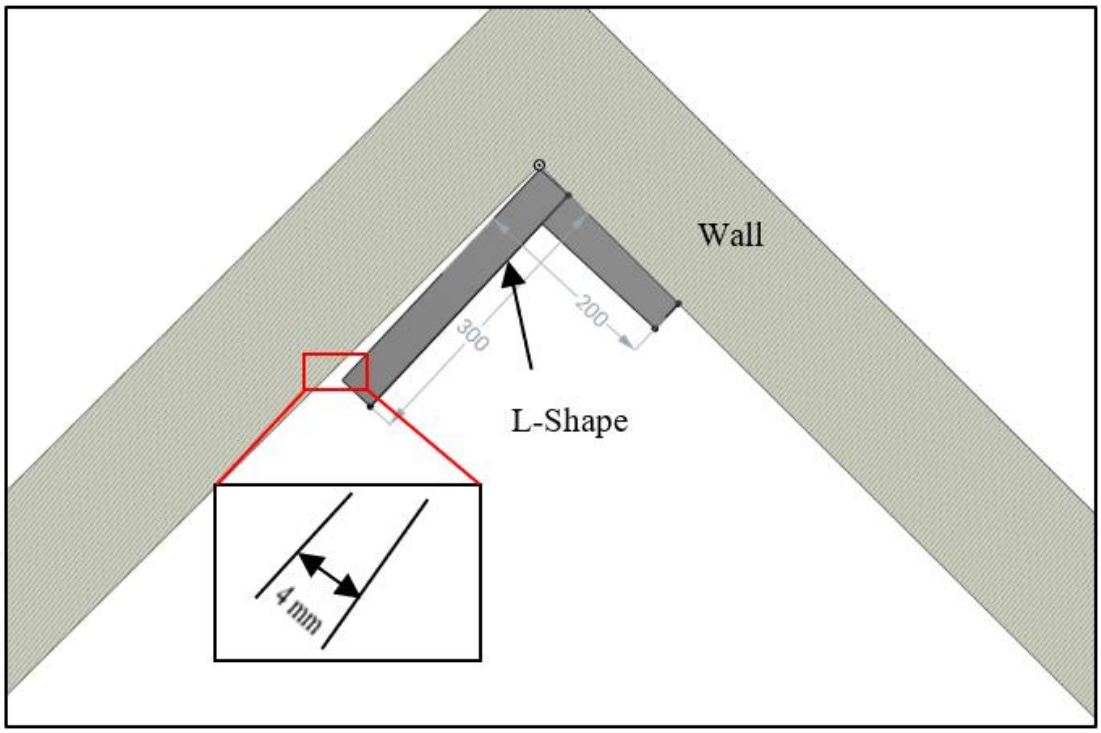

Figure 2. **Top View of Internal Wall Assessment.**

Equation (1) converts the 4 mm gap over the 300 mm L-square baseline into an ideal physical angular-deviation criterion of approximately 0.7639 degrees. This conversion does not mean that an angle measured directly in a perspective image is identical to the wall-to-wall angle. The apparent image angle is affected by lens distortion, camera intrinsics, camera pose, working distance, laser-plane orientation, and perspective. Accordingly, the 0.7639-degree value is treated as a future validation target rather than as demonstrated image-measurement performance.

CONSTRUCTION INSPECTION LITERATURE AND RESEARCH GAP

The recent literature confirms that automated quality inspection in construction is an established research field. QuicaBot integrates robotic mobility and sensing for building quality inspection (Yan et al., 2019), while a later on-site measuring robot addresses post-construction quality assessment (Wu et al., 2024). Depth sensing has been evaluated for wall evenness (Shukor et al., 2025), and streamlined laser scanning has been used for prefabricated wall-panel verticality (Wang et al., 2024). These studies show the value of controlled geometry and metric sensing, but they do not directly validate the proposed laser-line image workflow against the CIS 7 internal wall-corner rule.

Point-cloud research has automated segmentation, dimensional quality control, reconstruction, thinning, and virtual assembly for building components (Mirzaei et al., 2023; Yu et al., 2023; Kim and Lee, 2023; Jiang et al., 2023). Camera-pose control has also been identified as necessary when image-based three-dimensional reconstruction is used for prefabricated components (Lee et al., 2023). In parallel, UAV imagery has been mapped to BIM for external-wall inspection (Tan et al., 2022), and computer-vision applications in offsite construction have been reviewed across broader production tasks (Alsakka et al., 2023). These approaches establish relevant measurement principles while addressing targets, sensors, and acceptance rules different from the present wall-corner use case.

The bounded contribution of this paper is therefore a QLASSIC-specific synthesis connecting the 4 mm/300 mm criterion to image formation, calibration, laser-line extraction, angular resolution, uncertainty, and validation requirements. It does not claim that Canny edge detection, the Hough transform, robotic inspection, or optical construction measurement is itself novel. The intended contribution is the traceable translation of an existing manual acceptance rule into requirements for a future calibrated and experimentally validated workflow.

Table 2. Comparison of construction-quality inspection studies and relevance to the proposed QLASSIC workflow.

Study	Inspection target and method	Reported contribution	Relevance and boundary for this review
Yan et al. (2019)	QuicaBot robotic building inspection	Integrated robot for quality inspection and assessment	Foundational automated-inspection precedent; different sensing and validation scope
Tan et al. (2022)	UAV images linked to BIM for external walls	Mapped and modelled defect information	Shows image-to-BIM inspection integration; does not assess internal corner angle
Lee et al. (2023)	Camera-pose-aware inspection of prefabricated components	Addresses limitations of image-based 3D reconstruction	Supports explicit pose control and calibrated geometry
Mirzaei et al. (2023)	Point-cloud segmentation for dimensional control	End-to-end segmentation of building members	Demonstrates metric geometric inspection; sensor and target differ
Yu et al. (2023)	Point-cloud thinning for construction quality	Quality detection using nonuniform thinning	Relevant to efficient geometric data processing; no CIS 7 corner test
Kim and Lee (2023)	2D geometric reconstruction from point clouds	Automated model reconstruction for inspection	Supports geometry extraction from metric data
Jiang et al. (2023)	Point cloud and BIM for virtual trial assembly	Assesses prefabricated-structure fit	Shows traceable model-based comparison; different acceptance criterion
Alsakka et al. (2023)	Computer vision in offsite construction	Review of vision applications	Provides broader field context; not a wall-corner validation study
Johns et al. (2023)	Markerless vision for curtain-wall payload localisation	Localises crane payloads during installation	Shows construction-specific markerless vision; not a finished-wall quality test
Wu et al. (2024)	On-site measuring robot	Post-construction quality assessment	Recent robotic measurement precedent; no direct validation of this workflow
Wang et al. (2024)	Laser scanning of prefabricated wall panels	Streamlined verticality checking	Closest recent laser-based wall measurement; target is panel verticality
Shukor et al. (2025)	Depth-sensor wall-evenness evaluation	Building-quality measurement of wall surfaces	Locally relevant metric sensing; evaluates evenness rather than corner angle
Li et al. (2025)	High-precision building quality control	Review of advanced information technologies	Recent synthesis supporting precision and integration requirements
Present review	Future calibrated laser-line imaging for CIS 7 wall corners	Translates 4 mm/300 mm into calibration, resolution, uncertainty, and validation requirements	Conceptual synthesis only; hardware and experimental validation remain future work

CANDIDATE LASER-LINE IMAGE-PROCESSING WORKFLOW

The candidate workflow is derived from the construction-inspection evidence above and the technical foundations retained in Appendices A–D. It comprises controlled laser projection, calibrated image acquisition, distortion correction, edge-preserving preprocessing, Canny-based candidate-edge extraction, Hough-based line estimation, geometric conversion, uncertainty evaluation, and comparison with a traceable reference. Each stage remains a design proposition until the future hardware study is completed.

The following assertions represent the theoretical and conceptual inquiries made in developing the concept or strategy for a new wall alignment analysis. Appropriate studies, particularly in image processing steps, could be conducted in relation to the concepts and theories that have been established.

Theoretical Requirements

First, the suitable mechanism for assessing wall alignment according to CIS7 standards must be determined. Second, exploring various options for finding suitable methods is suggested when designing the image processing steps. Third, the practical technique to propose in developing the feature extraction process, especially the line details captured in the image. Finally, the best solution to improve the measurement accuracy for the proposed method can be determined.

Practical Hypotheses

First, a future implementation would project a calibrated laser plane across the two wall surfaces at the corner. The image-plane orientations of the resulting laser traces could be detected, but conversion to the physical wall-to-wall angle would require camera and laser-plane calibration, lens-distortion correction, controlled camera pose, and metric rectification or three-dimensional reconstruction. The horizontal laser line remains a candidate reference for future automated assessment alongside the L-square and steel-wedge procedure; its ability to replace the manual method has not yet been experimentally demonstrated.

Second, the assessment of wall alignment uses modern techniques, including a machine vision system for analyzing the captured image of the wall corner projected with the laser line. The important features of the images will be lines formed by the laser and the wall corner line. Image filtering and edge detection will be needed to enhance the line feature to be extracted.

Third, Hough Transform should be a suitable technique for extracting line features. This technique will produce an output that contains all the information regarding the lines detected from the image.

Fourth, the orientations and intersections of the detected image lines could be estimated from calibrated image data. These image-plane quantities should not be interpreted as the physical wall angle until the acquisition geometry has been calibrated and the measurement plane has been rectified or reconstructed. Intersection-finding methods such as K-means remain candidate extensions for future evaluation and cannot, by themselves, establish physical measurement accuracy.

Measurement Geometry and Resolution Requirements

Under the right-triangle interpretation of the manual L-square and steel-wedge procedure, the allowable gap g_lim over baseline L gives the physical angular-deviation criterion shown below:

$$\varepsilon_lim = \tan^{-1}(g_lim/L) \quad (2)$$

$$= \tan^{-1}(4/300) = 0.01333 \text{ rad} = 0.7639°$$

This value describes the physical geometry of the manual criterion. It does not define an allowable error for an uncalibrated image-processing output.

A perspective camera maps a three-dimensional point X to an image point x according to the calibrated pinhole

model:

$$\tilde{x} \sim K\,[R \mid t]\,\tilde{X} \tag{3}$$

where K contains the camera intrinsic parameters, while R and t describe the camera pose. Lens-distortion coefficients must also be estimated and applied before geometric measurement. Therefore, an angle formed by two lines in the raw image is an image-plane observable and is not generally equal to the physical wall-to-wall angle.

For a line detected using the polar Hough representation, its image parameters and direction may be expressed as:

$$\rho = u \cos\theta + v \sin\theta \tag{4}$$

$$\psi = \theta + \pi/2 \tag{5}$$

The angular separation between two detected image lines is:

$$\Delta\psi_img = \min(|\psi_1 - \psi_2|, \pi - |\psi_1 - \psi_2|) \tag{6}$$

The quantity $\Delta\psi_img$ remains an image-plane measurement. If the two wall planes have normal vectors n_1 and n_2, their physical dihedral angle α and deviation ε from perpendicularity are instead defined by:

$$\alpha = \cos^{-1}(|n_1^T n_2|/(\|n_1\|\|n_2\|)) \tag{7}$$

$$\varepsilon = |\pi/2 - \alpha| \tag{8}$$

Estimating α requires calibrated geometry. A future implementation could use a calibrated laser plane positioned perpendicular to the wall-corner direction and then apply metric rectification of that measurement plane, or it could reconstruct the laser traces in three dimensions. Because the two walls are non-coplanar, one planar homography cannot rectify both wall surfaces simultaneously; separate plane transformations or a calibrated three-dimensional model would be required.

Pixel resolution must be considered together with line length and localisation precision. For a detected line of length L_px pixels and approximate endpoint localisation uncertainty σ_px, a conservative planning approximation is:

$$\sigma_\theta \approx \sqrt{2}\,\sigma_px/L_px \quad \text{radians} \tag{9}$$

This relationship indicates that longer visible line segments and more precise subpixel localisation should reduce orientation uncertainty. An absolute minimum image resolution cannot be assigned until the field of view, working distance, stripe width, contrast, calibration accuracy, and localisation method have been established.

If the Hough accumulator samples orientation in increments of $\Delta\theta$, its approximate quantisation contribution and maximum single-line binning error are:

$$u_\theta, q = \Delta\theta/\sqrt{12}, \quad \text{maximum binning error} \approx \Delta\theta/2 \tag{10}$$

Because the acceptance criterion is approximately 0.7639 degrees, the angular sampling interval should be substantially smaller than this value. A preliminary interval of 0.1 degrees or finer is proposed for experimental evaluation, preferably followed by sub-bin peak estimation or line fitting using the detected edge coordinates. The 0.1-degree setting is a design candidate rather than a validated performance claim.

The eventual decision rule must be based on a combined uncertainty budget rather than on Hough resolution alone:

$$u_\varepsilon^2 \approx u_line1^2 + u_line2^2 + u_cal^2 + u_pose^2 + u_laser^2 + u_model^2 \tag{11}$$

The terms represent uncertainty from the two fitted lines, camera calibration, camera pose, laser-plane calibration, and the geometric model. Independence or covariance among these components must be evaluated during the future experimental study before compliance with the 0.7639-degree criterion can be assessed.

CONCLUSION AND FUTURE WORKS

The study defines and clarifies the issue within the existing wall alignment evaluation procedure. By comprehending the requirements and constraints of the existing process, a contemporary approach utilizing image processing becomes possible. As a result, projecting a laser line onto the wall corner is presented as a theoretical candidate for future automated assessment rather than as a demonstrated substitute for the conventional QLASSIC method. The approximately 0.76 degree value derived from the 4 mm over 300 mm criterion is treated as a future validation target, not as achieved performance. The fundamental idea of this unique approach is to analyze images collected using laser projection onto wall corners. This also includes a brief review of basic digital images, as this may assist in manipulating image data for our objectives. Besides, this study explores the potential existence of image noise, including photon and impulse noises, that could lead to unclear or noise issues during real-time image acquisition. Image filtering techniques such as linear and non-linear filters can be used to overcome the noise. Next, the edge detection method is a process of extracting valuable information from the laser line image. Finally, the Hough line transform is proposed for extracting line orientation, but its ability to support a physical compliance decision must be established through calibrated experiments.

This study is limited to a literature review and conceptual workflow. It does not report a completed laser-camera prototype, a real-wall dataset, camera calibration, measurement accuracy, repeatability, or agreement with the L-square and steel-wedge procedure. Future work will document the laser and camera hardware, working distance, field of view, image resolution, camera intrinsics, lens distortion, camera pose, laser-plane calibration, and acquisition conditions; test real or mock wall corners with traceable reference angles; perform repeated measurements; quantify angular error, combined uncertainty, and repeatability; evaluate a preliminary Hough angular interval of 0.1 degrees or finer together with sub-bin line refinement; and compare the image-based results with the QLASSIC manual assessment against the approximately 0.7639-degree criterion.

APPENDIX A. DIGITAL-IMAGE AND PIXEL-COORDINATE FOUNDATIONS

The material and figures in this appendix are retained from the original manuscript as technical background. They illustrate general image-processing concepts and do not constitute validation evidence for the proposed QLASSIC measurement workflow.

Based on the previous theoretical and conceptual syntheses, a vision system could be investigated as a candidate method for determining angle differences in future QLASSIC-oriented assessment. Its suitability for physical angle measurement will depend on camera calibration, controlled acquisition geometry, image resolution, uncertainty analysis, and experimental comparison with the manual procedure. The fundamentals of digital image definition and theory are outlined below.

Digital Image

From a machine learning standpoint, an image is a visual representation of the input data, and it may be dealt with simply by using computer vision techniques. A digital image is an image that has been digitized, which means that it has been transformed into a series of numbers that computers can comprehend (Kok et al., 2019).

*f(x,y),*Image digitization transforms the image into a computational form, where (x,y) is the picture element with units in pixels. The digital image may be in the binary form of 1-bit, 8-bit, or color (Sundararajan, 2017). An example of the transformation process from an analog image into a digital image is shown in Figure A1 below.

In many applications that compute digital images, The information pertaining to a digital image is typically saved either as a string or as an array of integers within the majority of the apps that calculate such images. In

addition to its more general uses, a digital image can be used for a wide variety of practical purposes. Some examples include implementations for medical tool analysis, machine vision systems, signal processing, and robotics through the use of image analysis techniques (Alhasan et al., 2021).

Before moving on to the numerous image modification methods and analyses required for this project, it is necessary first to understand the fundamental concept behind a digital image.

Pixel Coordinate System

Pixels are the elements that make up a digital image and are arranged in rows and columns. To access a pixel in a picture, we need to indicate the column and row in which it is placed to retrieve that pixel information. As shown in Figure A2, the columns represent the x-direction, numbered from left to right, while rows represent the y-direction, numbered from top to bottom. In this example, the pixel coordinates (2,3) indicate column number 2 and row number 3. Most vision software, such as OpenCV, OpenGL, and Cognex Vision Library (CVL), uses a numbering system starting from zero. In some cases, such as for MATLAB users, the number of rows and columns starts from one instead of zero.

Several types of applications are possible by implementing image coordinates, such as the image fusion technique, classification, and image clustering (Kumer et al., 2017; Chang et al., 2022; Mu et al., 2020; Davis et al., 1997). Other coordinate systems, such as the polar coordinate system, can be applied in the image processing method. This polar coordinate system can achieve coordinate measurement with higher efficiency, especially for rotational and complex curve measurements (Yin et al., 2022).

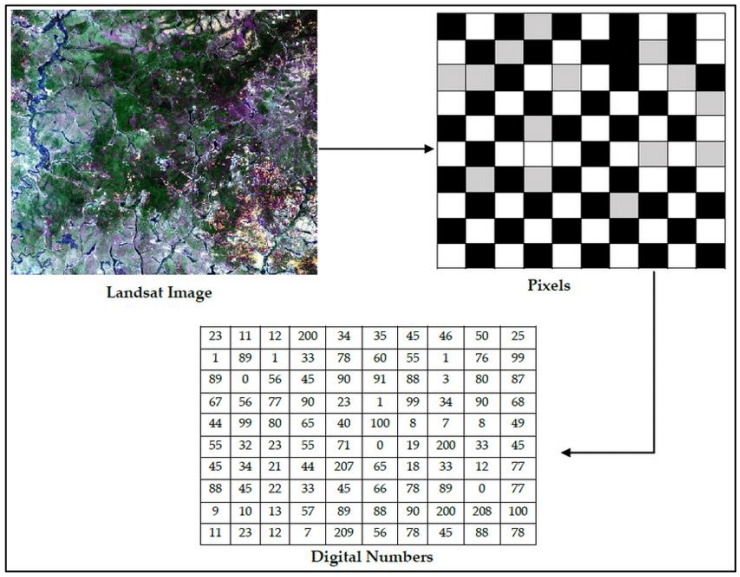

Figure A1. Digital Information Extracted from the Image (Phiri et al., 2017).

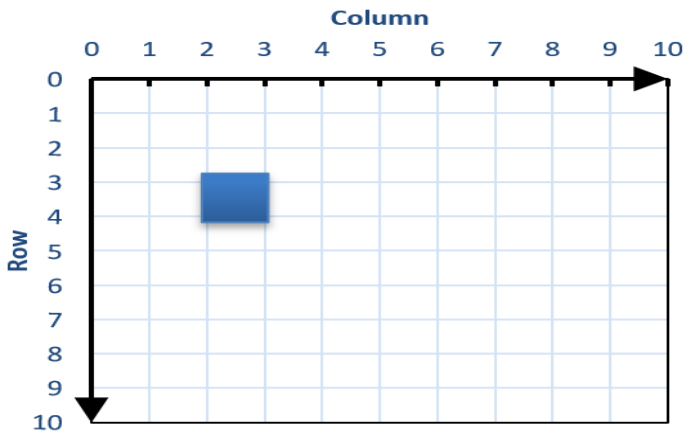

Figure A2. A 10 by 10 Pixel Grids Image.

For this project, pixel location knowledge must be acquired to analyze the point of interest discovered in the later stage. A setup of algorithm will have to be developed to analyze the laser lines projected onto the wall corner to inspect the wall alignment. The idea was to manipulate the pixel coordinates to match a particular point of the intersection between the laser lines.

APPENDIX B. IMAGE NOISE AND FILTERING FOUNDATIONS

The material and figures in this appendix are retained from the original manuscript as technical background. They illustrate general image-processing concepts and do not constitute validation evidence for the proposed QLASSIC measurement workflow.

The term "noise" refers to the variation or deviation of an image's brightness and color information. For a digital image, the noise may manifest itself in the form of pixel distortion, uneven lines, and blurred objects, among other things (Joshua et al., 2019). Several factors contribute to noise in images, such as environmental and lighting conditions, camera sensor temperature, transmission channel signal, or even the presence of dust. Noise can be categorized as shown in Figure B1.

Photon noise, also known as Shot or Poisson noise, occurs in an image due to the camera sensor's lack of photons detected. Shot noise is commonly present when the lighting conditions are poorly set up, resulting in a low lighting level. Thermal noise, known as Johnson-Nyquist noise, is detected in an image as white noise due to the random motion of electrons in any conducting medium.

Impulse noise mainly consists of Salt and Pepper noise. Both types of noise are produced as a result of signal transmission errors. There are certain cases where defective pixels in the sensor of the camera and faulty memory storage location could cause this type of noise (Win et al., 2019). Salt noise has a maximum grey level value of 255, which is the brightest, while pepper noise has a minimum grey level value of 0, which is the darkest. An example of salt and pepper noise is shown in Figure B2 below. Salt and pepper noise are usually dealt with by applying a median filter.

Understanding the noise characteristics and features is essential, as many wall images will be used for this project. The uneven and rough surface of the wall and sometimes holes or specks of dirt may be present in the wall image to be analyzed. These situations may lead to specific problems during the edge detection process and could also cause an error in the wall alignment inspection. Besides, noise could also present itself in the image due to other factors, such as poor lighting conditions and transmission signals. The correct methods for reducing image noise must be carefully selected to overcome these problems.

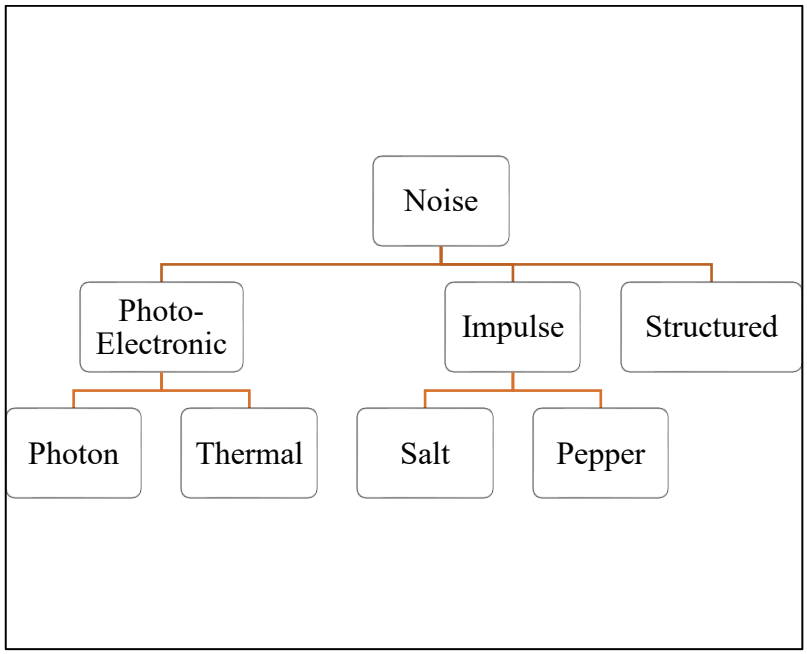

Figure B1. Image Noise Categories.

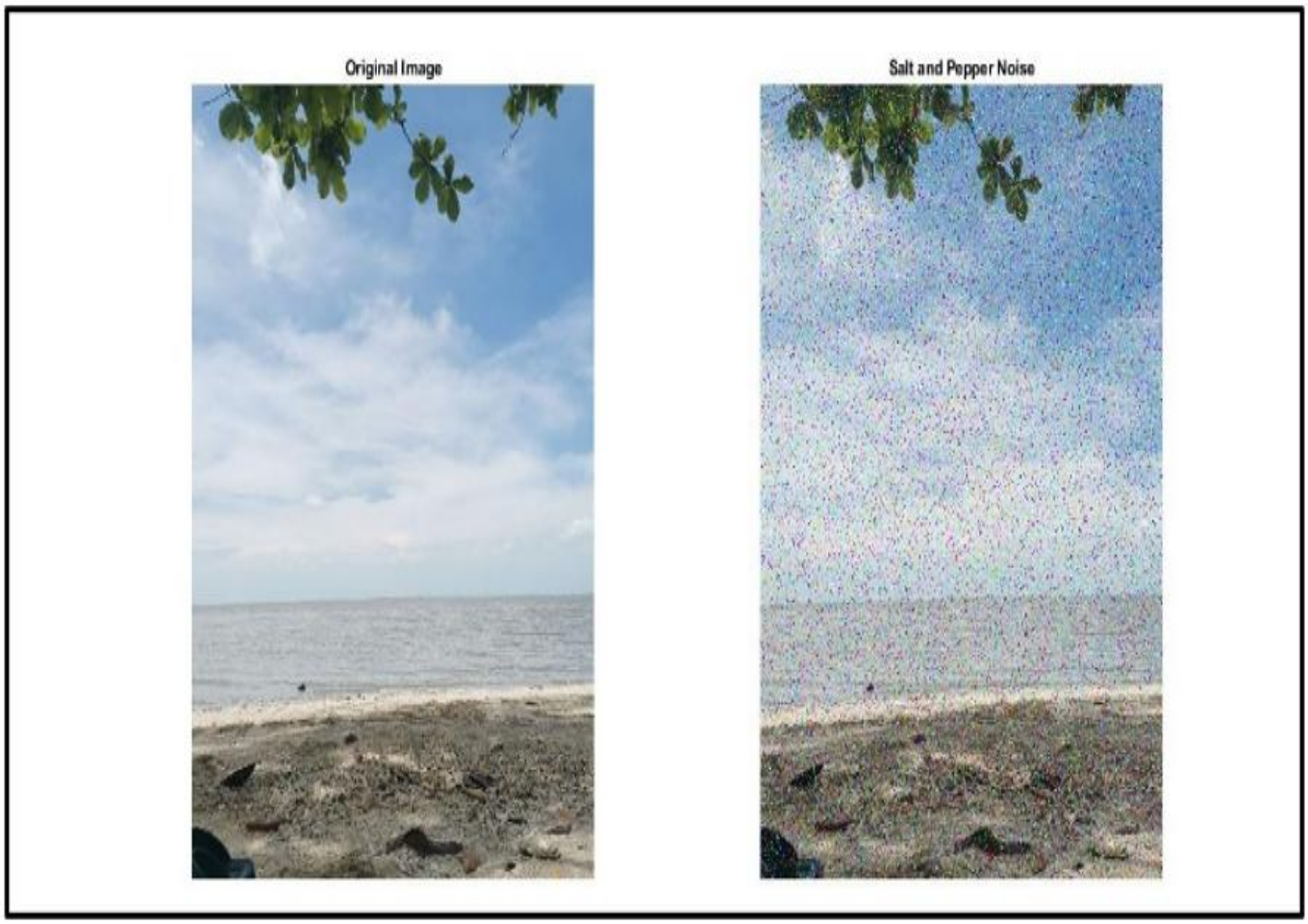

Figure B2. An Example of Salt and Pepper Noise in the Image.

IMAGE PROCESSING-FILTERING

Numerous techniques for digital image processing are available, depending on the task at hand. Some of these techniques include image editing, the Perona-Malik Diffusion, Principal Components Analysis, Linear Filtering, neural networks, pixelation, and methods based on partial differential equations (Ravikumar et al., 2019).

With the introduction of new technologies, it is possible to reach higher levels of accuracy, precision, and speed in image processing. Machine vision systems have been widely employed for scientific and industrial applications that require image analysis and inspection (Baghdadi et al., 2018; Ayub Khan et al., 2021).

The image filtering method is used to sharpen or blur the image depending on the desired result. Several image filters, such as spatial, temporal, and point operation filters, serve different purposes in image processing. Image filtering methods can be applied to reduce noise, hence boosting the feature extraction process of the image. The characterization of image features could be achieved using an appropriate filtering technique, such as wavelet filtering (Podulka, 2021).

Linear Filter

For linear filtering, a convolution kernel is needed to remove or reduce the target noise presented in the image. The resulting image will be filtered and blurred by performing a mathematical convolution of a kernel with an M x N size matrix on every pixel neighborhood and the center pixel (Davies, 2018; Semmlow, 2018). Thus reducing the unwanted noise from the image. The two-dimensional convolution of the image can be represented as:

$$u(x,y)=F(x,y)*I(x,y) \quad (12)$$

$$u(x,y)=\sum_{j=-N}^{N}\sum_{i=-M}^{M}F(i,j)I(x-i,y-j) \quad (13)$$

where *u(x,y)* is the output convolution at a point *(x,y)*, *I* is the impulse response, and *F(i,j)* is the input signal. For discrete functions, the equation can be expressed as:

The mean filter is one of the common types of linear filtering methods. This filter uses a uniform weight average mask across the image. This method is practical for averaging the amount of intensity of all pixels in the image. However, this method is unsuitable for this project application because it creates boxy image artifacts.

In contrast, the Gaussian filter applies a weighted average filter to the input image. However, the output image will have a smoothing and filtering effect that comes at the cost of blurry details of edges and lines present in the image. In this case, the Gaussian filter works well on the flat region of the image but not with the edge's region. The Gaussian spatial size filter can be expressed as:

$$w_s(u,v)=e^{-\frac{(u-x)^2+(v-y)^2}{2\sigma_s^2}} \quad (14)$$

where $w_s(u,v)$ is the spatial neighborhood smoothing factor, and σ_s is the Gaussian spatial parameter standard deviation (Kafadar, 2022). Increasing the σ_s increases the smoothing size window, thus increasing the blurred effect.

Non-Linear Filter

The median filter is a non-linear filter that reduces the image's noise while preserving the edges. The concept of the median filter is to replace the center of the output sample with the median of all neighboring pixels. However, using this method, the Gaussian noise, which usually occurs in an electrical system, will not be removed (Solovyeva, 2019; Kaur et al., 2021). Besides, the computational complexity of median filters is a significant downside. Figure B3 depicts a comparison of the mean, median, and Gaussian filters.

The bilateral filter works by adopting the Gaussian linear filter principle with the combination of Gaussian spatial mask control and brightness range mask (Geng et al., 2020). The bilateral filter is an enhanced non-linear filtering technique that can be easily implemented using OpenCV software (Li et al., 2022). Two factors concerning the bilateral filter can be expressed as:

$$w_s(u,v)=e^{-\frac{(u-x)^2+(v-y)^2}{2\sigma_s^2}} \quad (15)$$

$$w_t(u,v)=e^{-\frac{\|g(u,v)-g(x,y)\|^2}{2\sigma_t^2}} \quad (16)$$

where $w_s(u,v)$ is the spatial information from the Gaussian filter, $w_t(u,v)$ is the brightness difference measured in grayscale, and Sigma,σ_t is the standard deviation of the intensity difference. Increasing both parameters increases the chance of removing the critical features of the image. Therefore, a proper range for both parameters σ_s and σ_t must be carefully selected to maximize the result. Other methods of improving the bilateral filter include robust bilateral and optimized bilateral filters (Asokan et al., 2020; Routray et al., 2020).

Anisotropic diffusion is a direction-independent image filtering method that can reduce noise while also maintaining distinguishing features of the image, such as edges and lines. However, several studies have been conducted to improve this method, as it has proved to be inefficient when applied to an image containing impulse noise. In some cases, the filter has over-smoothing the output image (Chen et al., 2017; Mishra et al., 2018; Nair et al., 2019). In the end, this project will have to focus more on analyzing the laser line segment to evaluate the alignment of the wall corner. Therefore, a simple but practical filter option must be chosen to apply to this project.

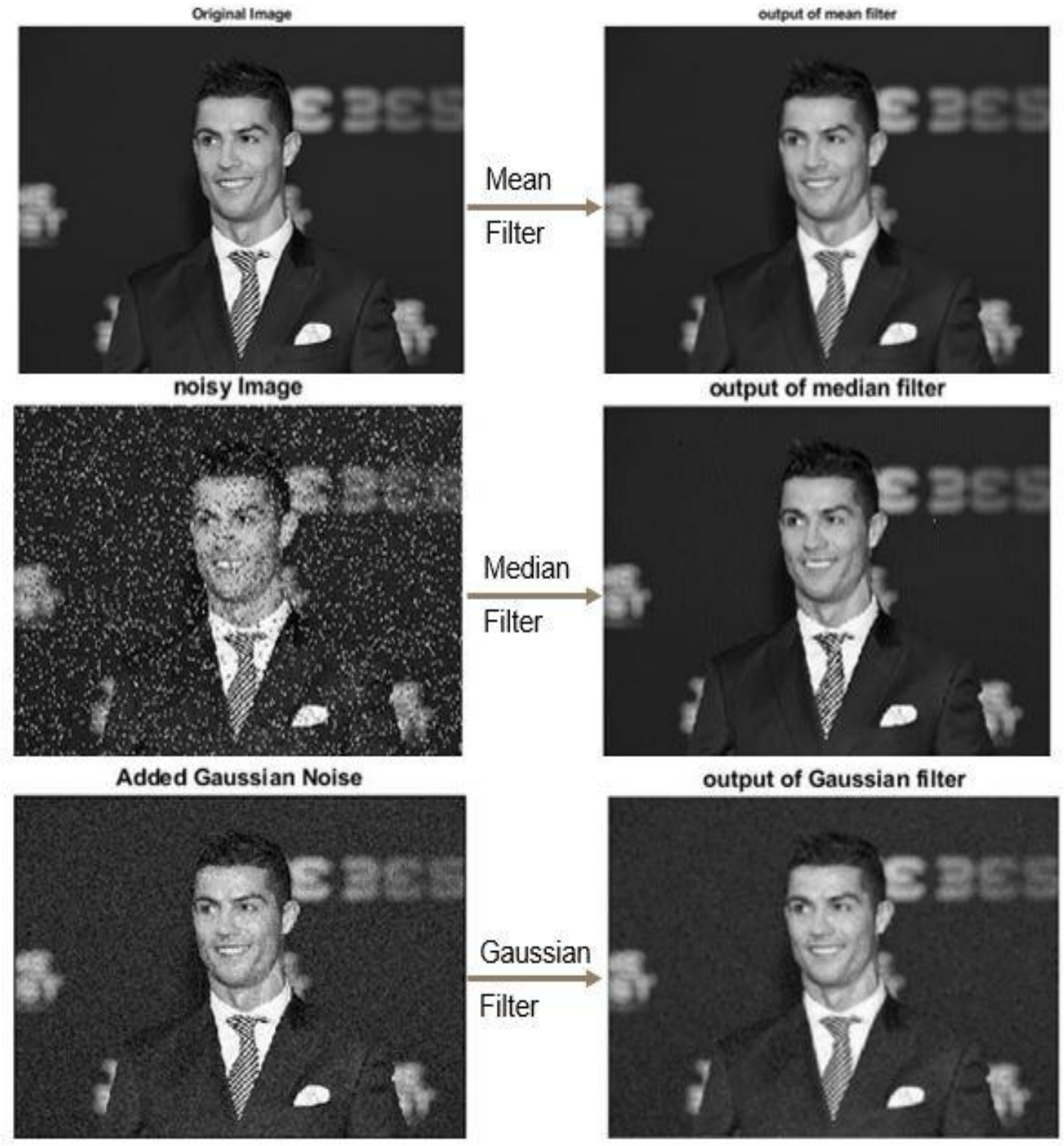

Figure B3. Comparison Between Mean, Median, and Gaussian Filter.

APPENDIX C. EDGE-DETECTION FOUNDATIONS

The material and figures in this appendix are retained from the original manuscript as technical background. They illustrate general image-processing concepts and do not constitute validation evidence for the proposed QLASSIC measurement workflow.

For this project, the laser will be projected onto the corner of the wall, and the alignment of the line can be analyzed for further evaluation. For extracting the line features, the details of the line segment must be appropriately extracted so that the desired edges present in the image are preserved. For that purpose, relevant

edge operators were considered to obtain information regarding the edges, such as their position, magnitude, and orientation. The most common operators for edge detectors are the gradient operator and the Laplacian operator (Yang et al., 2022).

Gradient Operator

Roberts, Prewitt, and Sobel operators were elemental examples of gradient edge detectors. Usually, the masking of the edges in the image could be achieved by implementing a threshold to the convolved image. This type of operator implemented the first derivative of the image in their operation in the x and y directions. The local extrema found by solving the first derivative of the continuous gradient function in each direction indicates the position of the edges on the image. The local maxima were identified by converting the gradient function's derivative into an absolute value that contained the magnitude of the edge. Lastly, by using these two pieces of information, the orientation of the edges can be determined. A two-dimensional image as a function f with the value of pixel's intensity *(x,y)* can be described as:

$$\nabla f(x,y) = \left[\frac{\partial f}{\partial x}, \frac{\partial f}{\partial y} \right] \tag{17}$$

$$\| \nabla f(x,y) \| = \sqrt{\left(\frac{\partial f}{\partial x} \right)^2 + \left(\frac{\partial f}{\partial y} \right)^2} \tag{18}$$

$$\theta = tan^{-1} \left(\frac{\partial f}{\partial x} / \frac{\partial f}{\partial y} \right) \tag{19}$$

$\nabla f(x,y)$ $\frac{\partial f}{\partial x}$ $\frac{\partial f}{\partial y}$ $\| \nabla f(x,y) \|$ where is the gradient vector, is the derivative in the x-direction, is the derivative in the y-direction, is the magnitude of the gradient, and θ is the direction of the gradient (Sun et al., 2020). Three pieces of information regarding the edge could be obtained using the gradient function operator. However, this method may produce unwanted results, such as discontinued lines, noise, and inaccuracy, leading to errors in the edge segmentation process (Samat et al., 2020; Fang et al., 2019, Ono, 2017, Prasath et al., 2020). The development of multi-scale gradient maps and minimized gradient functions could improve the gradient operator. Technically, the smoothing operation had to be done before the edge detection operation on the image was performed. Most of the edge operators discussed in this section already embedded the smoothing process in each operation. Figure C1 demonstrates the gradient operator process.

Laplacian Operator

The Laplacian operator applied the first derivative of the Gaussian filter to smooth the image before convolving the image with the Laplacian of Gaussian (LoG) to find zero-crossing. The process was commonly known as the Mexican Hat operator. By applying the second derivative, edges were transformed into zero-crossing, which yielded the edge's location and image enhancement (Ding et al., 2017). The above statement of LoG can be described in the equation below:

$$\nabla^2 f(x,y) = \left[\frac{\partial^2 f}{\partial x^2}, \frac{\partial^2 f}{\partial y^2} \right] \tag{20}$$

The LoG is said to have a quick response to a sudden change in the image, hence was proposed to be used to detect seismic activities (Saad et al., 2018). Figure C2 demonstrates the Laplacian operator process, in which the method has some disadvantages, such as providing only the location of the edges while also having high sensitivity to noise, similar to the case of the gradient operator.

Canny Edge Operator

With the Canny edge operator, the image will be filtered by the Gaussian derivative. Next, the Sobel operator will be applied to the smoothed image. Any gradient operator could achieve this purpose as long as the output contained the information for the gradient magnitude of the image. In that case, the edges' magnitude and orientation will be found, and a smoothed image will be the output.

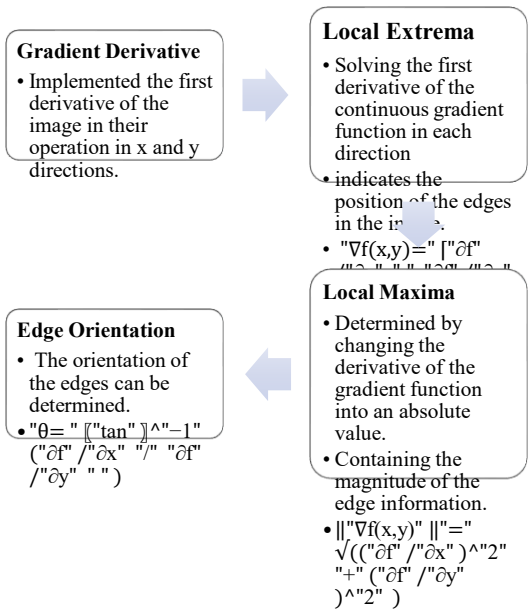

Figure C1. Gradient-Based Operator Overall Process.

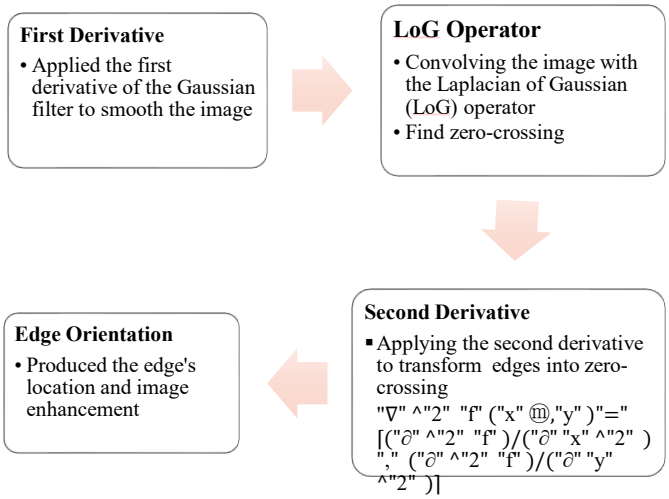

Figure C2. Laplacian-Based Operator Overall Process.

The process involved calculating the edge gradient G and the orientation of the gradient θ for every pixel. The denoted gradient can be described as:

$$G=\sqrt{G_x^{\,2}+G_y^{\,2}} \tag{2}$$

$$\theta=tan^{-1}\left(\frac{G_x}{G_y}\right) \tag{3}$$

$G_x G_y$where and represent, respectively, the edge gradient in the horizontal and vertical directions. Next, the non-maximum suppression technique proceeds onto the image to derive thin edges from the thick edges present in the image. The edge will be detected by performing the hysteresis threshold, where the maximum and minimum values are defined (Ratsakou et al., 2020). The non-relevant pixels would also be detected using this method. The working principle for the Canny edge detector is presented in Figure C3 below. Also, Figure C4 demonstrates the Canny Edge operator process.

The performance of different edge operators was compared, as shown in Figure C5, and the Canny edge detector

was preferred to be used but with some limitations. The Canny operator was found to have discontinued edges and a longer computing time (Hu et al., 2022; Huang et al., 2022; Yang et al., 2021).

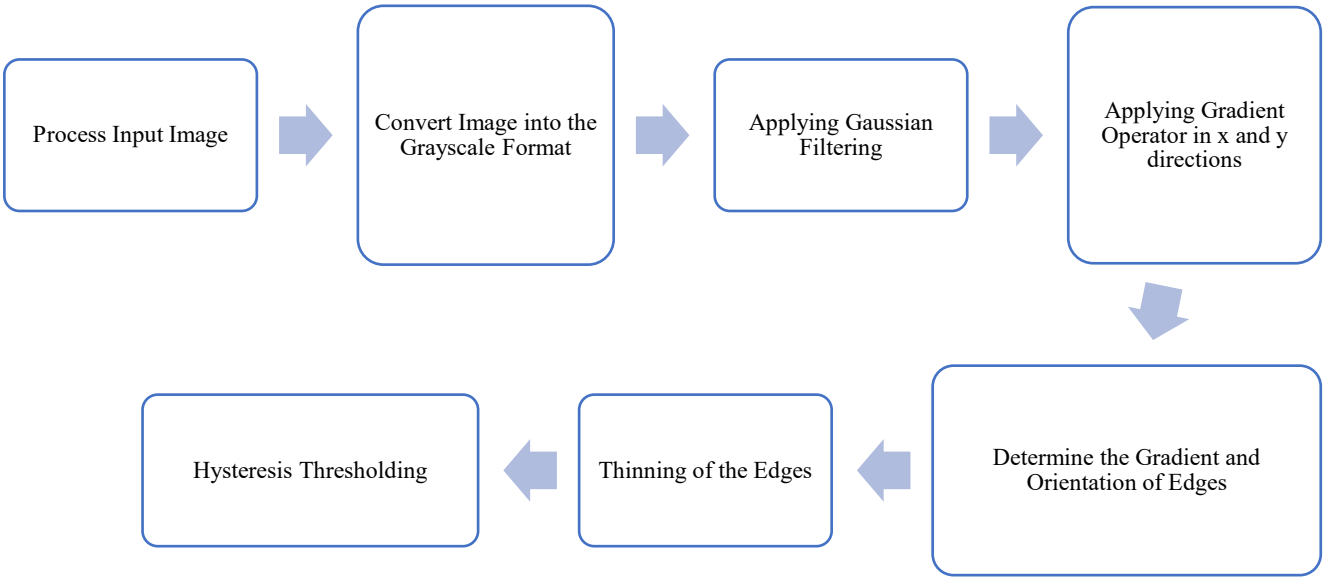

Figure C3. Canny Edge Operator Process.

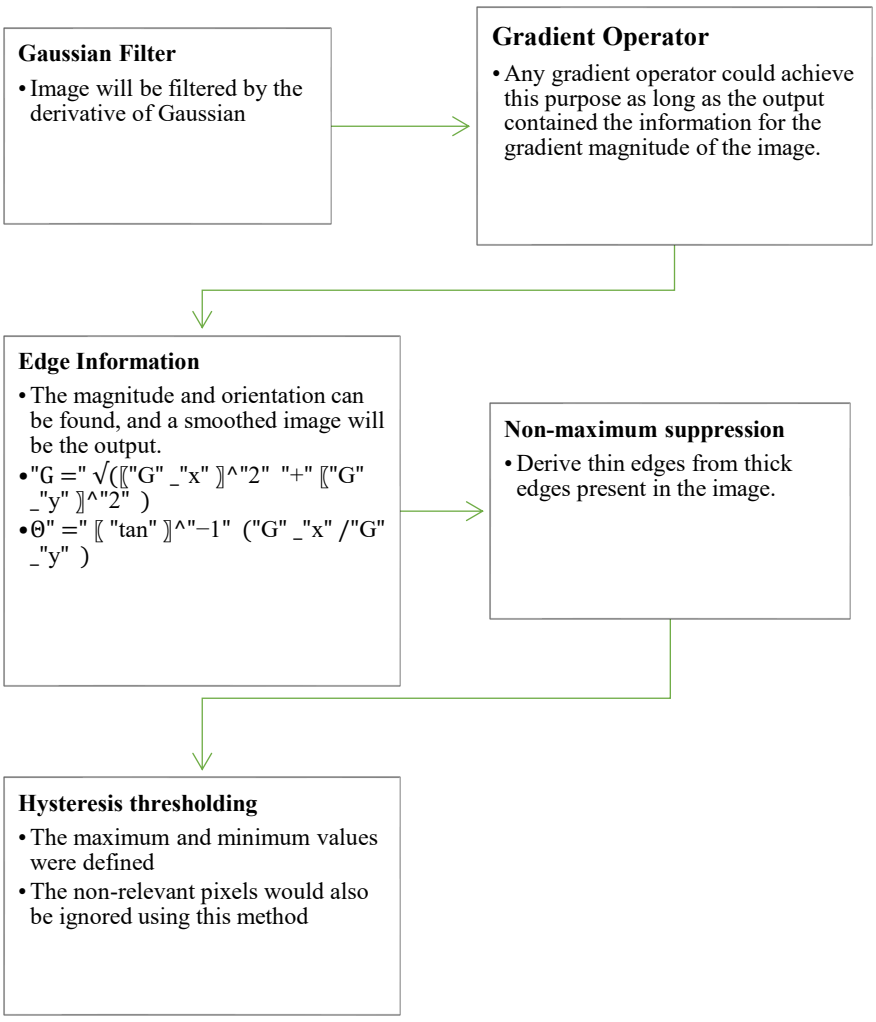

Figure C4. Canny Edge-Based Operator Overall Process.

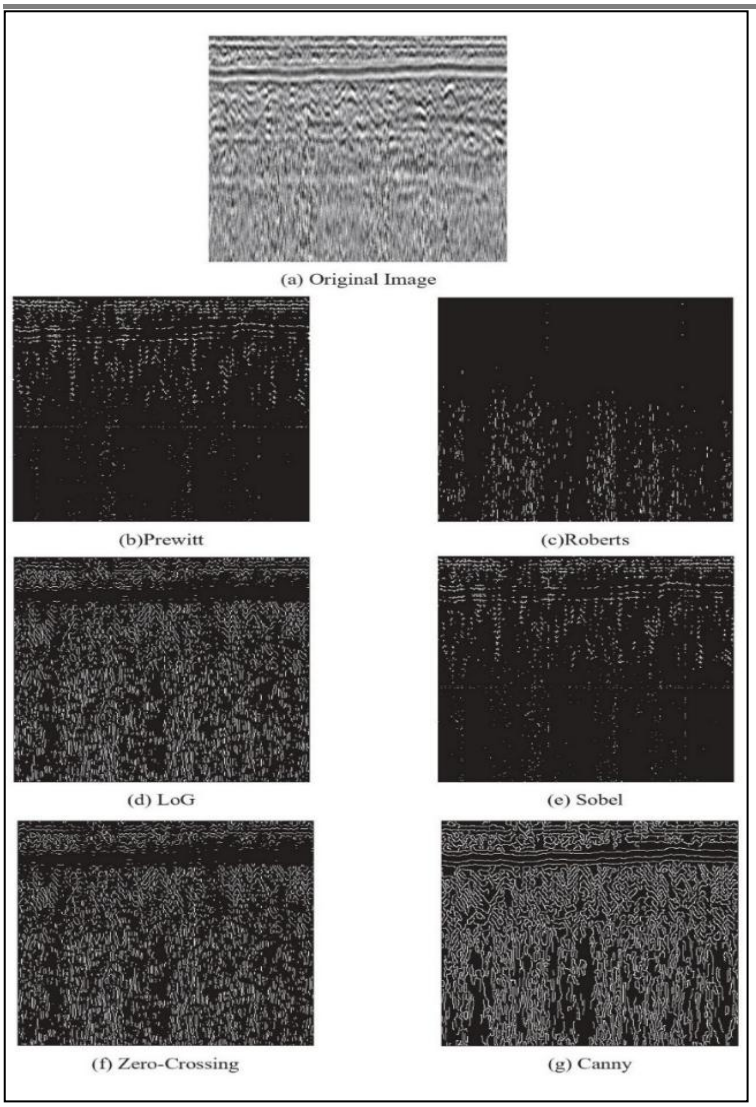

Figure C5. Edge Detection using Different Operators (Yang et al., 2021).

Edge detection using the Canny edge operator produced an output image with the most edge details intact. Gradient-based operators such as Prewitt, Sobel, and Roberts produced output images with diminished details of the edges present in the original image. The Laplacian of Gradient (LoG) operator and zero-crossing operator preserve the edge details but with some blurry effects. The proposed method of assessing wall alignment will rely heavily on the details of the wall corner's vertical line and supposedly horizontal laser lines. If the line details were blurred during the image filtering process, then the output angle difference obtained from the line features will be affected, as blurry lines will cause the lines to appear bigger than the actual size.

Thus, the Canny-Edge operator was the suitable choice for this project, but some modifications have to be made to the parameters used in the program. Thus, only important line features will be extracted from the image. Using the Canny-Edge operator could also increase the chance of eliminating unwanted details on the wall surfaces, such as dust, dirt, small holes, or uneven surfaces.

APPENDIX D. HOUGH-TRANSFORM FOUNDATIONS

The material and figures in this appendix are retained from the original manuscript as technical background. They illustrate general image-processing concepts and do not constitute validation evidence for the proposed QLASSIC measurement workflow.

Hough Transform (HT) is a feature extraction method widely used for computer vision and image processing applications. HT is insensitive toward the image noise and has tolerance in detecting the discontinuity of edges. The Hough transform can detect lines and circles in Hough Space by implementing voting concepts using the

parametric form. A line equation y can represent a line in an image, where *m* and *b* denote the slope of the line detected and the *Y*-intercept, respectively. The HT uses polar coordinates to define the line in parametric form. For any given edge point (x_i,y_i), the first equation below shows the line equation in Cartesian coordinates, while the second equation shows the line equation in (ρ,θ) polar coordinates.

$$y = mx + b \tag{4}$$

$$\rho = x\cos\theta + y\sin\theta \tag{5}$$

where ρ represents the perpendicular distance from the origin to the line, while θ indicates the angle formed by the horizontal axis and the vector perpendicular to the line on a 2D plane (Wang, 2019), the statement above can be represented as shown in Figure D1.

$\theta\rho - \rho + \rho\rho(\rho,\theta)(x_i,y_i)$The angle ranges between 0 and 180 degrees, while the radius ranges between and , where is the diagonal length of the edge on the image. In parametric form, the pair corresponds to a straight line that passes through the edge point . The line detection in HT uses slope-intercept for the voting process, as shown in Figure D2. A sinusoidal waveform represents pixels in a line, whereas the intersection point of that sinusoidal curve indicates the pixels resting on the same line.

The basic steps included in HT are described below:

- Step 1: Edge points (x_i,y_i) were extracted from the image and mapped to polar coordinates to compute a set of straight lines that pass through the edge point.
- Step 2: Hough Transform applied to edge points, represented in the sinusoidal waveform, where the same pixels on a line corresponding to the intersection point indicate a probable line.
- Step 3: An accumulator in Hough Space inspects the index for the pair of (θ,ρ) that matches. Next, the accumulator's value will be incremented.
- Step 4: The pair of (θ,ρ) with a voting value more significant than a specified threshold was considered as a line.
- Step 5: The starting and ending points of the defined line can be determined. Inverse Hough Transform returns the two endpoint coordinates.
- Step 6: The length of the line was then calculated. If the length of the line is greater than the pre-determined threshold, the line will be considered an output.

The HT standard architecture for detecting and showing lines is demonstrated in Figure D3. Note that HT uses complex computational capacity while requiring ample memory space. Therefore, an improved algorithm was introduced that gives the HT the ability to extract boundary lines in real-time accurately (Wang, 2020). However, HT can also be used with the Canny Edge operator to solve simple problems requiring less complex computation, such as measuring the skew angle between lines (Edun et al., 2021; Tong et al., 2018).

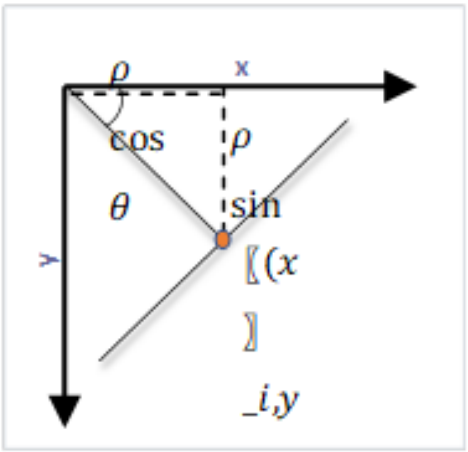

Figure D1. Hough Transform on the x-y Plane.

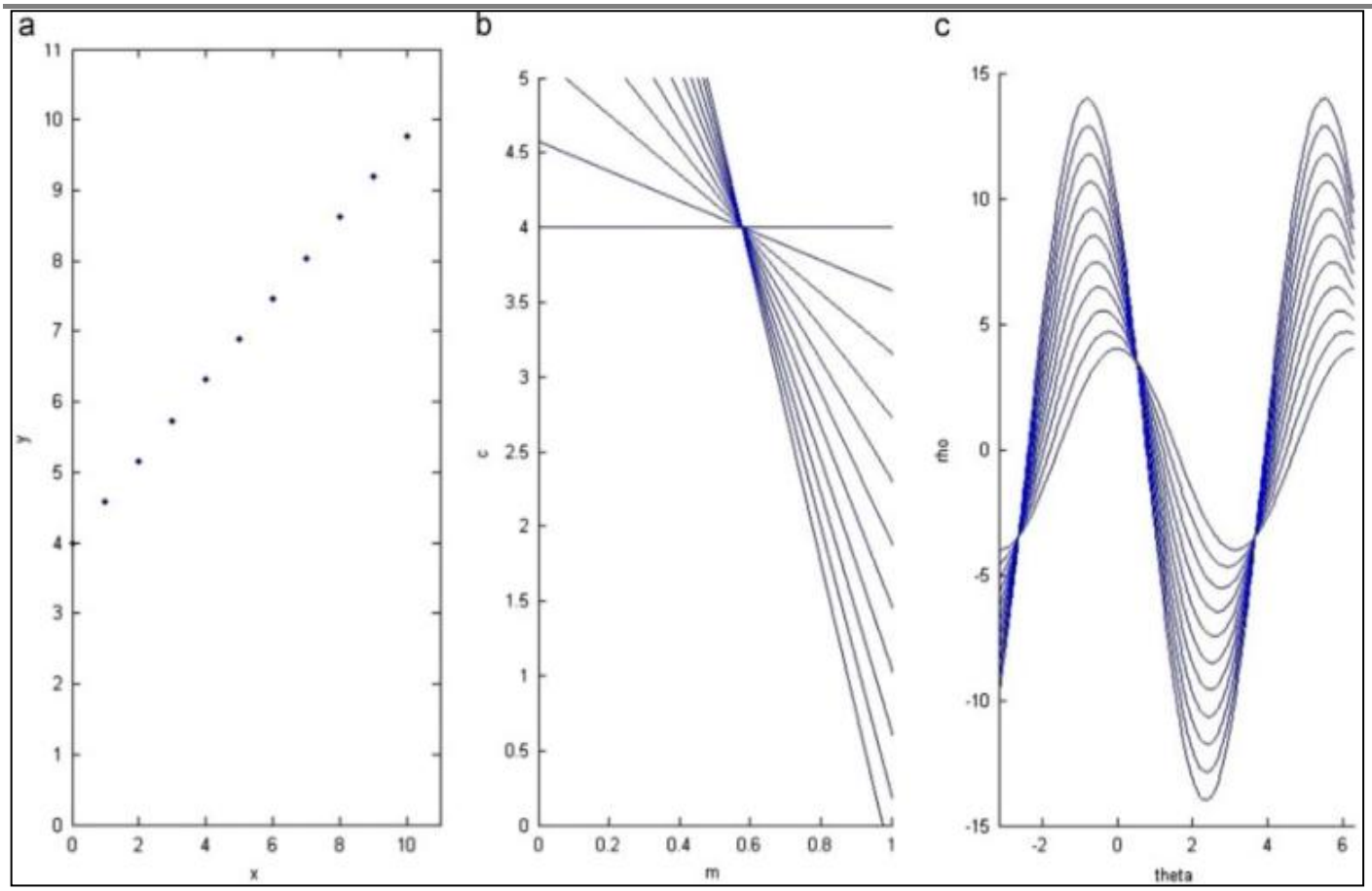

Figure D2. HT Line Detection. (a) A Group of Symmetrical Points in the Image "(x,y)" plane. (b) The slope Intercept in Parameter Space "(m,b)" -Plane. (c) A Set of Sinusoidal Curves in Parameter "(θ,ρ)" -Plane (Mukhopadhyay et al., 2015).

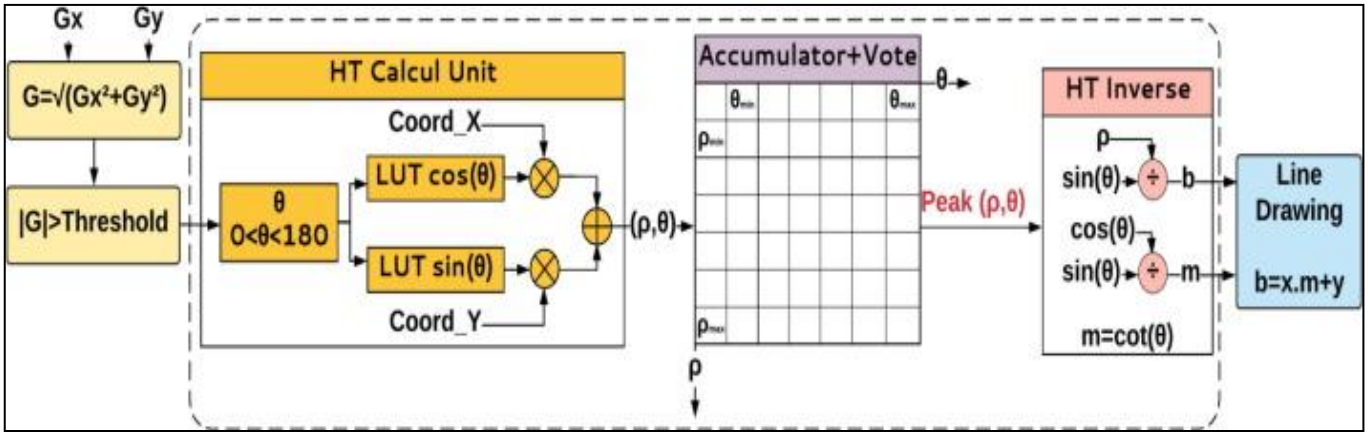

Figure D3. Standard Hough Transform Architecture (el Hajjouji et al., 2020).

ACKNOWLEDGMENT

The authors would like to acknowledge the support by Universiti Teknikal Malaysia Melaka (UTeM) for performing the study. The authors would also like to convey our credits to the Robotics and Industrial Automation research group of the Faculty of Electrical Technology and Engineering.

REFERENCES

1. Alhasan, M., Hasaneen, M. (2021). Digital imaging, technologies, and artificial intelligence applications during COVID-19 pandemic. *Computerized Medical Imaging and Graphics*, vol. 91, p. 101933. doi:

10.1016/J.COMPMEDIMAG.2021.101933.

2. Alsakka, F., Assaf, S., El-Chami, I., Al-Hussein, M. (2023). Computer vision applications in offsite construction. Automation in Construction, 154, 104980. doi: 10.1016/j.autcon.2023.104980.
3. Arnaud, A., Gouiffes, M., Ammi, M. (2018). On the Fly Plane Detection and Time Consistency for Indoor Building Wall Recognition Using a Tablet Equipped with a Depth Sensor. *IEEE Access*, vol. 6, pp. 17643–17652. doi: 10.1109/ACCESS.2018.2817838.
4. Asokan, A., Anitha, J. (2020). Adaptive Cuckoo Search based optimal bilateral filtering for denoising of satellite images. *ISA Transactions*, vol. 100, pp. 308–321. doi: 10.1016/J.ISATRA.2019.11.008.
5. Ayub Khan, A., Laghari, A., Awan, S., Lyari, P. Karachi. (2021). Machine Learning in Computer Vision: A Review. *ICST Transactions on Scalable Information Systems*. doi: 10.4108/eai.21-4-2021.169418.
6. Baghdadi, A., Hussein, A., Ahmed, Y., Cavuoto, L., Guru, K. (2018). A Computer Vision Technique for Automated Assessment of Surgical Performance using Surgeon Console-feed Videos. *International Journal of Computer Assisted Radiology and Surgery*, vol. 14, pp. 697–707. doi: 10.1007/s11548-018-1881-9.
7. Chang, J.-H., Leung, Y.-C. (2022). Dynamic image clustering from projected coordinates of deep similarity learning. *Neural Networks*. doi: https://doi.org/10.1016/j.neunet.2022.03.030.
8. Cheah, C. C., et al. (2021). Guest Editorial Introduction to the Focused Section on Mechatronics and Automation for Constructions. *IEEE/ASME Transactions on Mechatronics*, vol. 26, no. 6, pp. 2819–2825. doi: 10.1109/TMECH.2021.3127237.
9. Chen, H., Feng, J., Zhou, B., Hu, Y., Guo, K. (2017). An Anisotropic Diffusion-Based Dynamic Combined Energy Model for Seismic Denoising. *IEEE Geoscience and Remote Sensing Letters*, vol. 14, no. 7, pp. 1061–1065. doi: 10.1109/LGRS.2017.2695649.
10. Construction Industry Development Board Malaysia. (2021). *Quality Assessment System for Building Construction Works*. Accessed: May 19, 2022. [Online]. Available: www.cidb.gov.my
11. Davies, E. R. (2018). Image filtering and morphology. *Computer Vision*, pp. 39–92. doi: 10.1016/B978-0-12-809284-2.00003-4.
12. Davis, M. H., Khotanzad, A., Flamig, D. P., Harms, S. E. (1997). A physics-based coordinate transformation for 3-D image matching. *IEEE Transactions on Medical Imaging*, vol. 16, no. 3, pp. 317–328. doi: 10.1109/42.585766.
13. Ding, K., Xiao, L., Weng, G. (2017). Active contours driven by region-scalable fitting and optimised Laplacian of Gaussian energy for image segmentation. *Signal Processing*, vol. 134, pp. 224–233. doi: 10.1016/J.SIGPRO.2016.12.021.
14. Edun, A. S., Perry, K., Harley, J. B., Deline, C. (2021). Unsupervised azimuth estimation of solar arrays in low-resolution satellite imagery through semantic segmentation and Hough transform. *Applied Energy*, vol. 298, p. 117273. doi: 10.1016/J.APENERGY.2021.117273.
15. el Hajjouji, I., Mars, S., Asrih, Z., el Mourabit, A. (2020). A novel FPGA implementation of Hough Transform for straight lane detection. *Engineering Science and Technology, an International Journal*, vol. 23, no. 2, pp. 274–280. doi: 10.1016/J.JESTCH.2019.05.008.
16. Fang, S., Yao, Z., Zhang, J. (2019). Scale and gradient aware image smoothing. *IEEE Access*, vol. 7, pp. 166268–166281. doi: 10.1109/ACCESS.2019.2953550.
17. Geng, J., Jiang, W., Deng, X. (2020). Multi-scale deep feature learning network with bilateral filtering for SAR image classification. *ISPRS Journal of Photogrammetry and Remote Sensing*, vol. 167, pp. 201–213. doi: 10.1016/J.ISPRSJPRS.2020.07.007.
18. Hu, X., Wang, Y. (2022). Monitoring coastline variations in the Pearl River Estuary from 1978 to 2018 by integrating Canny edge detection and Otsu methods using long time series Landsat dataset. *CATENA*, vol. 209, p. 105840. doi: 10.1016/J.CATENA.2021.105840.
19. Huang, M., Liu, Y., Yang, Y. (2022). Edge detection of ore and rock on the surface of explosion pile based on improved Canny operator. *Alexandria Engineering Journal*, vol. 61, no. 12, pp. 10769–10777. doi: 10.1016/J.AEJ.2022.04.019.
20. Jiang, Y., Shu, J., Ye, J., Zhao, W. (2023). Virtual trail assembly of prefabricated structures based on point cloud and BIM. Automation in Construction, 155, 105049. doi: 10.1016/j.autcon.2023.105049.
21. Johns, B., Abdi, E., Arashpour, M. (2023). Crane payload localisation for curtain wall installation: A markerless computer vision approach. Measurement, 221, 113459. doi: 10.1016/j.measurement.2023.113459.

22. Joshua, O., Ibiyemi, T., Adu, B. (2019). A Comprehensive Review On Various Types of Noise in Image Processing. *International Journal of Scientific and Engineering Research*, vol. 10, pp. 388–393.
23. Kafadar, Ö. (2022). Applications of the Kuwahara and Gaussian filters on potential field data. *Journal of Applied Geophysics*, vol. 198, p. 104583. doi: 10.1016/J.JAPPGEO.2022.104583.
24. Kaur, M., Sarkar, R. K., Dutta, M. K. (2021). Investigation on quality enhancement of old and fragile artworks using non-linear filter and histogram equalisation techniques. *Optik (Stuttg)*, vol. 244, p. 167564. doi: 10.1016/J.IJLEO.2021.167564.
25. Kim, M., Lee, D. (2023). Automated two-dimensional geometric model reconstruction from point cloud data for construction quality inspection and maintenance. Automation in Construction, 154, 105024. doi: 10.1016/j.autcon.2023.105024.
26. Kok, C.-W., Tam, W.-S. (2019). Digital Image. *Digital Image Interpolation in Matlab*, IEEE, pp. 17–70. doi: 10.1002/9781119119623.ch2.
27. Kumer, S. V. A., Srivatsa, S. K. (2017). A compilation of image fusion process using decision-based coordinates of an image. *2017 IEEE International Conference on Power, Control, Signals and Instrumentation Engineering (ICPCSI)*. pp. 2338–2342. doi: 10.1109/ICPCSI.2017.8392135.
28. Lee, D., Nie, G.-Y., Han, K. (2023). Vision-based inspection of prefabricated components using camera poses: Addressing inherent limitations of image-based 3D reconstruction. Journal of Building Engineering, 64, 105710. doi: 10.1016/j.jobe.2022.105710.
29. Li, C. Z., Zeng, J., Tam, V. W. Y., Wu, H. (2025). Advanced information technologies for high-precision quality control in building engineering. Journal of Building Engineering, 101, 111918. doi: 10.1016/j.jobe.2025.111918.
30. Li, Z., Fang, X., Yang, G. (2022). Remove adversarial perturbations with linear and non-linear image filters. *Displays*, vol. 73, p. 102143. doi: 10.1016/J.DISPLA.2021.102143.
31. Mirzaei, K., Arashpour, M., Asadi, E., Masoumi, H., Mahdiyar, A., Gonzalez, V. (2023). End-to-end point cloud-based segmentation of building members for automating dimensional quality control. Advanced Engineering Informatics, 55, 101878. doi: 10.1016/j.aei.2023.101878.
32. Mishra, D., Chaudhury, S., Sarkar, M., Soin, A. S., Sharma, V. (2018). Edge Probability and Pixel Relativity-Based Speckle Reducing Anisotropic Diffusion. *IEEE Transactions on Image Processing*, vol. 27, no. 2, pp. 649–664. doi: 10.1109/TIP.2017.2762590.
33. Mu, C., Liu, J., Liu, Y., Liu, Y. (2020). Hyperspectral Image Classification Based on Active Learning and Spectral-Spatial Feature Fusion Using Spatial Coordinates. *IEEE Access*, vol. 8, pp. 6768–6781. doi: 10.1109/ACCESS.2019.2963624.
34. Mukhopadhyay, P., Chaudhuri, B. B. (2015). A survey of Hough Transform," *Pattern Recognition*, vol. 48, no. 3, pp. 993–1010. doi: 10.1016/J.PATCOG.2014.08.027.
35. Nair, R. R., David, E., Rajagopal, S. (2019). A robust anisotropic diffusion filter with low arithmetic complexity for images. *Eurasip Journal on Image and Video Processing*, vol. 2019, no. 1, pp. 1–14. doi: 10.1186/S13640-019-0444-5/TABLES/5.
36. Olanrewaju, A., Tan, Y. Y., Soh, S. N. (2021). Defect characterisations in the Malaysian affordable housing. *International Journal of Building Pathology and Adaptation*, vol. ahead-of-print, no. ahead-of-print. doi: 10.1108/IJBPA-11-2018-0095.
37. Ono, S. (2017). L0 Gradient Projection. *IEEE Transactions on Image Processing*, vol. 26, no. 4, pp. 1554–1564. doi: 10.1109/TIP.2017.2651392.
38. Phiri, D., Morgenroth, J. (2017). Developments in Landsat land cover classification methods: A review. *Remote Sensing*, vol. 9, no. 9. doi: 10.3390/rs9090967.
39. Podulka, P. (2021). Application of image processing methods for the characterisation of selected features and wear analysis in surface topography measurements. *Procedia Manufacturing*, vol. 53, pp. 136–147. doi: 10.1016/J.PROMFG.2021.06.018.
40. Prasath, V. B. S., Thanh, D. N. H., Hung, N. Q., Hieu, L. M. (2020). Multi-scale Gradient Maps Augmented Fisher Information-Based Image Edge Detection. *IEEE Access*, vol. 8, pp. 141104–141110. doi: 10.1109/ACCESS.2020.3013888.
41. Ratsakou, A., Skarlatos, A., Reboud, C., Lesselier, D. (2020). Shape reconstruction of delamination defects using thermographic infrared signals based on an enhanced Canny approach. *Infrared Physics & Technology*, vol. 111, p. 103527. doi: 10.1016/J.INFRARED.2020.103527.

42. Ravikumar, R., Arulmozhi, V. (2019). Digital Image Processing-A Quick Review. *International Journal of Intelligent Computing and Technology (IJICT)*, vol. 2, no. 2, pp. 11–19.
43. Routray, S., Malla, P. P., Sharma, S. K., Panda, S. K., Palai, G. (2020). A new image denoising framework using bilateral filtering based non-subsampled shearlet transform. *Optik (Stuttg)*, vol. 216, p. 164903. doi: 10.1016/J.IJLEO.2020.164903.
44. Saad, O. M., Shalaby, A., Samy, L., Sayed, M. S. (2018). Automatic arrival time detection for earthquakes based on Modified Laplacian of Gaussian filter. *Computers & Geosciences*, vol. 113, pp. 43–53. doi: 10.1016/J.CAGEO.2018.01.013.
45. Samat, A., Li, J., Lin, C., Liu, S., Li, E. (2020). Edge Gradient-Based Active Learning for Hyperspectral Image Classification. *IEEE Geoscience and Remote Sensing Letters*, vol. 17, no. 9, pp. 1588–1592. doi: 10.1109/LGRS.2019.2951800.
46. Semmlow, J. (2018). Two-Dimensional Signals—Basic Image Analysis. *Circuits, Signals, and Systems for Bioengineers*, pp. 491–526. doi: 10.1016/B978-0-12-809395-5.00011-4.
47. Shukor, A. Z., Zailani, M. A., Jamaluddin, M. H., Ramli, M. Z., Omar, G., Abd Ghani, S. H. (2025). Evaluation of wall evenness using depth sensor for building quality assessment. Jurnal Teknologi, 88(1), 65–74. doi: 10.11113/jurnalteknologi.v88.23439.
48. Solovyeva, E. (2019). Cascade Non-linear Filters for Image Recovery. *Procedia Computer Science*, vol. 150, pp. 109–115. doi: 10.1016/J.PROCS.2019.02.023.
49. Song, W., Liu, L., Yifei, T., Sun, G., Fong, S., Cho, K. (2017). A 3D localisation method in indoor environments for virtual reality applications. *Human-centric Computing and Information Sciences*, vol. 7. doi: 10.1186/s13673-017-0120-7.
50. Spencer, B. F., Hoskere, V., Narazaki, Y. (2019). Advances in Computer Vision-Based Civil Infrastructure Inspection and Monitoring. *Engineering*, vol. 5, no. 2, pp. 199–222. doi: https://doi.org/10.1016/j.eng.2018.11.030.
51. Sun, J., Lv, Y., Tang, C., Sima, H., Wu, X. (2020). Face Recognition Based on Local Gradient Number Pattern and Fuzzy Convex-Concave Partition. *IEEE Access*, vol. 8, pp. 35777–35791. doi: 10.1109/ACCESS.2020.2975312.
52. Sundararajan, D. (2017). Digital image processing: A signal processing and algorithmic approach. *Digital Image Processing: A Signal Processing and Algorithmic Approach*, pp. 1–468. doi: 10.1007/978-981-10-6113-4.
53. Tan, Y., Li, G., Cai, R., Ma, J., Wang, M. (2022). Mapping and modelling defect data from UAV captured images to BIM for building external wall inspection. *Automation in Construction*, vol. 139, p. 104284. doi: https://doi.org/10.1016/j.autcon.2022.104284.
54. Tan, Y., Li, S., Liu, H., Chen, P., Zhou, Z. (2021). Automatic inspection data collection of building surface based on BIM and UAV. *Automation in Construction*, vol. 131, p. 103881. doi: https://doi.org/10.1016/j.autcon.2021.103881.
55. Tong, J., Shi, H., Wu, C., Jiang, H., Yang, T. (2018). Skewness correction and quality evaluation of plug seedling images based on Canny operator and Hough transform. *Computers and Electronics in Agriculture*, vol. 155, pp. 461–472. doi: 10.1016/J.COMPAG.2018.10.035.
56. Wang, J., Fu, P., Gao, R. X. (2019). Machine vision intelligence for product defect inspection based on deep learning and Hough transform. *Journal of Manufacturing Systems*, vol. 51, pp. 52–60. doi: 10.1016/J.JMSY.2019.03.002.
57. Wang, L., Gu, X., Liu, Z., Wu, W., Wang, D. (2022). Automatic Detection of Asphalt Pavement Thickness: a Method Combining GPR Images and Improved Canny Algorithm. *Measurement*, p. 111248. doi: 10.1016/J.MEASUREMENT.2022.111248.
58. Wang, L., Yang, Y., Shi, J. (2020). Measurement of harvesting width of intelligent combine harvester by improved probabilistic Hough transform algorithm. *Measurement*, vol. 151, p. 107130. doi: 10.1016/J.MEASUREMENT.2019.107130.
59. Wang, M., Wang, C. C., Zlatanova, S., Shen, X., Brilakis, I. (2024). A streamlined laser scanning verticality check method for installation of prefabricated wall panels. Journal of Construction Engineering and Management, 150(11), 04024159. doi: 10.1061/JCEMD4.COENG-14989.
60. Win, N., Kyaw, K., Win, T., Aung, P. (2019). Image Noise Reduction Using Linear and Non-linear Filtering Techniques. *International Journal of Scientific and Research Publications (IJSRP)*, vol. 9, p. p92113. doi: 10.29322/IJSRP.9.08.2019.p92113.

61. Wu, H., Ma, M., Yang, Y., Han, L., Wu, S. (2024). On-site measuring robot technology for post-construction quality assessment of building projects. Buildings, 14(10), 3085. doi: 10.3390/buildings14103085.
62. Yan, R. J., Kayacan, E., Chen, I. M., Tiong, L. K., Wu, J. (2019). QuicaBot: Quality Inspection and Assessment Robot. *IEEE Transactions on Automation Science and Engineering*, vol. 16, no. 2, pp. 506–517. doi: 10.1109/TASE.2018.2829927.
63. Yang, D., Peng, B., Al-Huda, Z., Malik, A., Zhai, D. (2022). An overview of edge and object contour detection. *Neurocomputing*, vol. 488, pp. 470–493. doi: 10.1016/J.NEUCOM.2022.02.079.
64. Yang, Y., Zhao, X., Huang, M., Wang, X., Zhu, Q. (2021). Multispectral image-based germination detection of potato by using supervised multiple threshold segmentation models and Canny edge detector. *Computers and Electronics in Agriculture*, vol. 182, p. 106041. doi: 10.1016/J.COMPAG.2021.106041.
65. Yap, J. B. H., Tan, C. W., Loo, S. C., Lee, W. P. (2020). Towards a 'branded' property developer: key traits for Malaysian housing market. *International Journal of Housing Markets and Analysis*, vol. 12, no. 4, pp. 626–643. doi: 10.1108/IJHMA-06-2018-0039.
66. Yin, P., Han, F., Wang, J., Lu, C., Du, H. (2022). Influence of coordinate system establishment error on tooth profile deviation measured by standard polar coordinate method on gear measuring center. *Measurement*, vol. 187, p. 110344. doi: https://doi.org/10.1016/j.measurement.2021.110344.
67. Yu, J., Wu, G., Wu, W., Ma, W., Chang, H., Wei, Z., Jiang, X., Xu, J. (2023). Construction quality detection based on point cloud nonuniform thinning method. Structures, 56, 104930. doi: 10.1016/j.istruc.2023.104930.